EES Batteries

ROYAL SOCIETY OF CHEMISTRY

PAPER

View Article Online
View Journal

Cite this: DOI: 10.1039/d5eb00104h

Origin of enhanced disorder in high entropy rocksalt type Li-ion battery cathodes

Lin Wang,†[a] You Wang,†[b] Jayden Martin,†[b] Elena Scivally,[a] Zhengda He,[a] Do-hoon Kim,[c] Dong-hee Yeon,[c] Yan Zeng,[a] Dongchang Chen*[b] and Bin Ouyang *[a]

Received 27th May 2025,
Accepted 21st August 2025

DOI: 10.1039/d5eb00104h

rsc.li/EESBatteries

High entropy disordered rocksalt (HE-DRX) structure has emerged as a new platform for achieving high energy density and high-rate performance while minimizing the use of critical metals, *e.g.* Co and Ni. Recent studies have shown that high-entropy compositions can reduce detrimental chemical short-range order, making Li more extractable during electrochemical process. However, the factors that control the degree of disorder in HE-DRX remain unknown. In this work, we demonstrate that pronounced cation disorder arises from deviation in lattice distortion and cation charge states. Furthermore, we observe an inverse correlation between the tendency for disorder and the phase stability of specific HE-DRX materials, indicating a trade-off between disordering tendency with structural stability. These design principles are based on data mining 18 810 DFT computed HE-DRX compositions with different orderings, encompassing 28 typical cation species used in cathodes. Experimental comparisons of two materials with the same theoretical redox capacity but different tendencies for disorder further validate our theoretical predictions regarding both phase stability and disordering tendency. The design principles proposed in this work will refine the roadmap for discovering high-rate, earth-abundant Li-ion battery cathodes with optimized short-range order.

Broader context

Developing sustainable energy-storage cathodes that avoid critical metals is vital for expanding renewable-energy technologies while easing supply-chain pressures. High-entropy disordered rocksalt (HE-DRX) materials offer a cost-effective option: their intrinsic cation disorder suppresses detrimental short-range order and accelerates Li-ion transport. Yet the origin of this disorder remains unclear. Mining a dataset of 18 810 DFT-computed compositions, we show that large off-lattice distortions and the absence of high-valence cations are the chief drivers of disorder in HE-DRX cathodes. Raman spectroscopy and electrochemical Li-extraction tests validate these design rules, linking the identified structural features to improved ionic accessibility.

1. Introduction

Developing earth-abundant cathode materials for Li-ion batteries has become a critical challenge for the electrified future, particularly with the rapid development of the EV industry, which highlights the urgency of addressing supply chain issues. One promising strategy is to reduce or eliminate the use of critical metals, *e.g.* Co and Ni, by incorporating multiple principle elements.[1,2] This concept has been successfully applied to disordered rocksalt (DRX) type Li-ion battery cathodes. Recent discoveries[1,3,4] suggest that high entropy disordered rocksalt (HE-DRX) cathodes can offer competitive capacity and energy density compared to commercial Li-ion battery cathodes.[5,6] Moreover, it has been found out that the presence of multiple principal elements increases lattice randomness, enhancing ion percolation and reducing the detrimental chemical short-range order (SRO) commonly found in DRX cathodes.[1,4,7–11] These early efforts suggest significant potential for developing cost-effective cathodes that do not rely on specific critical metals like Co and Ni.

As HE-DRX type cathodes continue to evolve, one unsettled puzzle is the physical origin of enhanced disorder and the reduction of SRO features. In this work, we present our understanding of the control handles that promote more disordered HE-DRX candidates through an extensive computational dataset for data mining. Specifically, we developed a dataset of 18 810 DFT-computed materials, encompassing two different

[a]Department of Chemistry and Biochemistry, Florida State University, Tallahassee, FL 32304, USA. E-mail: bouyang@fsu.edu
[b]Department of Chemistry and Chemical Biology, The University of New Mexico, Albuquerque, NM 87131, USA. E-mail: chend@unm.edu
[c]Samsung SDI, Yeongtong-gu, Suwon-si, Gyeonggi-do, 16678, Korea
†These authors contribute equally to this work.

disordering states (*e.g.* fully random and state with chemical short-range order), Li contents, F concentrations and 28 potential metal species. Through data mining, we have discovered that the enhanced disorder is more frequently observed in structures with greater off-lattice distortion and those with absence of high valence metals. To validate these predictions, we synthesized two representative HE-DRX compositions with same redox capacities but distinct predicted disorder tendencies. Both were characterized by X-ray diffraction, Rietveld refinement, and Raman spectroscopy to confirm structural integrity and local disorder. Electrochemical measurements, including galvanostatic cycling and GITT, were conducted under identical conditions. The HE-DRX with higher disorder tendency indeed shows higher Li extractability. Based on these findings, we have refined the design principles for creating HE-DRX materials with more pronounced disorder, helping to narrow the design space for high-rate, earth-abundant Li-ion battery cathodes.

2. Methods

2.1. Special quasi-random structure (SQS)

Special quasi-random structures (SQSs) are periodic structures whose atomic distributions are selected such that the cluster correlations approach the expected value in a random atomic arrangement as closely as possible for a given structure size.[12,13] Given this feature, SQSs are an appropriate choice for investigating the properties of rocksalt materials with full disorder. Our previous studies on DRXs using SQSs also indicate that these structures can be effective tools for quantifying phase stability,[1,14] electronic structure[15] and voltage curves.[16,17]

2.2. DFT calculations

First-principles DFT calculations were performed to obtain an accurate description of the structural energies and oxidation states of the different cathode materials. All the calculations were performed using the projector-augmented wave (PAW) method[18] as implemented in the Vienna *Ab initio* Simulation Package (VASP).[19] A rotationally averaged Hubbard U correction[20,21] was used to correct the self-interaction error in oxides containing Cr, Fe, Mn, Mo, and V. The U parameters were obtained from a previously reported calibration to oxide formation energies.[21] For all calculations, a reciprocal space discretization of 25 k-points per $Å^{-1}$ was applied, with a plane-wave cutoff energy of 520 eV, and the convergence criteria were set as 10^{-6} eV for electronic loops and 0.02 eV $Å^{-1}$ for ionic loops. With the DFT relaxation, the lattice distortion deviated from rigid lattice, which is an important feature of high entropy materials, will be automatically captured by local energy minimization.

2.3. Thermodynamic stability

The thermodynamic stability was evaluated by constructing the convex hull of the DFT total energy for all phases in the relevant chemical space available in Materials project[22] which contains phases from the Inorganic Crystal Structure Database (ICSD) and some compounds generated using data-mined substitution rules.[23] The same DFT calculations were used to determine the energies of those competing phases from the Materials project,[22] ensuring consistency in the evaluation of phase stability. The convex hull ensures that each ground state has an energy lower than any linear combination of phases that leads to the same composition as the ground state. Phase stability for phases not on the hull is quantified by their energy above the hull (E_{hull}), which indicates the compound's driving force for decomposition into other ground states. E_{hull} serves as a reasonable indicator of synthetic accessibility, as experimentally accessible materials must generally have a low E_{hull} value.[24–26] To estimate the synthetic accessibility, we also apply ideal mixing entropy into the E_{hull} computed at 0 K, which yields $E_{hull,1473K} = E_{hull,0K} - 1473S_{Ideal}$. The use of 1473 K is to consider the typical upper bound of solid-state synthesis temperature.

2.4. Synthesis and characterizations

All chemicals for synthesis were purchased commercially and used without further purification. The HE-DRX compounds were synthesized by the solid-state reaction. For $Li_{21}Mg_2Ti_3Zr_3Mn(III)_2Mn(IV)_2Fe_3O_{36}$, stoichiometric amounts of Li_2CO_3 (Sigma-Aldrich, ≥99.0%), MgO (Beantown Chemical, 99%), $Zr(OH)_4$ (Sigma-Aldrich, 97%), TiO_2 (Sigma-Aldrich, 99.0%), Mn_2O_3 (Sigma-Aldrich, 99.0%), MnO_2 (Alfa Aesar, 98%), and Fe_2O_3 (Thermo Fisher Scientific, 99.9%) mix with ethanol at 200 rpm for 18 h in a planetary ball mill (Retsch PM 200). To compensate for the Li loss in high-temperature calcination process, 10% extra Li_2CO_3 was added. The mixture was dried at 80 °C for 24 h, then grinded as fine powders. Then the powders were calcined at 950 °C for 12 h in an argon-atmosphere quartz tube furnace, with a ramping rate of 5 °C min^{-1}. By replacing the TiO_2 with Nb_2O_5 (Sigma-Aldrich, 99.9%) and the same subsequent procedures, $Li_{21}Mg_3Zr_3Mn(III)_2Nb_3Fe_4O_{36}$ can be obtained. X-ray diffraction (XRD) of samples was collected *via* a Rigaku SmartLab X-ray diffractometer (Cu Kα, 40 kV, 40 mA). A Ni-foil Cu Kβ filter was inserted to filter out most of the Kβ diffraction peaks.

2.5. Electrochemical measurements

Cathode active materials were first ball-milled with acetylene carbon black (Denka) with a mass ratio of 6 : 3 in 300 rpm for 12 hours. Then the ball milled composite was mixed with polyvinylidene fluoride (PVDF) binder in a 9 : 1 weight ratio in an *N*-methyl-2-pyrrolidone (NMP, Sigma-Aldrich, 99.7%) solvent. The slurry was cast onto an aluminum foil using a 150 μm doctor blade and dried overnight at 100 °C under vacuum, through which electrode with thickness of ~100 μm can be generated. The loading density of active material is approximately 2–3 mg cm^{-2}. Type-2032-coin cells (half-cell configuration) were assembled in an argon-filled glove box without calendaring. The architecture of the coin cell is consistent with literature reported previously.[27] A Li foil (Sigma Aldrich,

700 μm in thickness, diameter: 1.43 cm) was used as the counter/reference electrode and two Celgard 2325 tri-layer microporous membranes were used as the separator. A solution of 1 M $LiPF_6$ in 1 : 1 (v/v) ethylene carbonate (EC): diethylene carbonate (DEC) (PuriEL) was used as the electrolyte. The amount of electrolyte is 75 μL. The total mass of each coin cell, including all components (*i.e.* gasket, spring washer, cell cases), is approximately 3.7 g. The electrochemical properties of the coin cells were tested *via* a Neware Battery Testing System in the voltage range of 1.5–4.8 V with a current density of 10 mA g^{-1} at room temperature. Approximately 2–3 cells were fabricated for each type of electrode and each current density for cycling tests to minimize the random errors.

3. Results

3.1. High throughput screening, compositional coverage and ordering consideration

The compositional space for high-throughput screening spans 13 elements and 28 species, as shown in Fig. 1(a). To sample typical Li contents and F concentrations, six prototype formulas, *e.g.*, $Li_{48}M_{32}O_{80}$, $Li_{48}M_{32}O_{64}F_{16}$, $Li_{21}M_{15}O_{36}$, $Li_{21}M_{15}O_{30}F_6$, $Li_{24}M_{12}O_{30}F_6$ and $Li_{24}M_{12}O_{24}F_{12}$ are selected based on typical reported compositions of DRX.[8,9,28,29] This set captures a representative range of Li content and F concentrations. In DRX cathodes, the Li content typically ranges from 1.0 to 1.333 per two anions, balancing improved Li percolation (favored by higher Li content) against greater metal redox capacity (favored by lower Li content and thus higher metal content).[9,30] Similarly, the F content generally falls between 0.0 and 0.333 per two anions, balancing higher synthesizability (associated with lower F content) against greater metal redox capacity (associated with higher F content).[9,30,31] Our selection of Li and F contents therefore provides good coverage of the typical compositional ranges observed in DRX systems. At fixed Li content and F concentration, we have enumerated all possible compositions that have six metal species while the stoichiometry is chosen to ensure the maximized entropy. While five or more cations in near-equimolar ratios is a common approximation for "high-entropy",[2] we incorporate at least six metals with closest stoichiometry they can reach under the constraint of charge balance. For each composition, we ordered the cations by minimizing the Ewald summation, denoted as electrostatic ground state (ESGS), *e.g.*, ESGS structures or by approximating the probability of clusters to

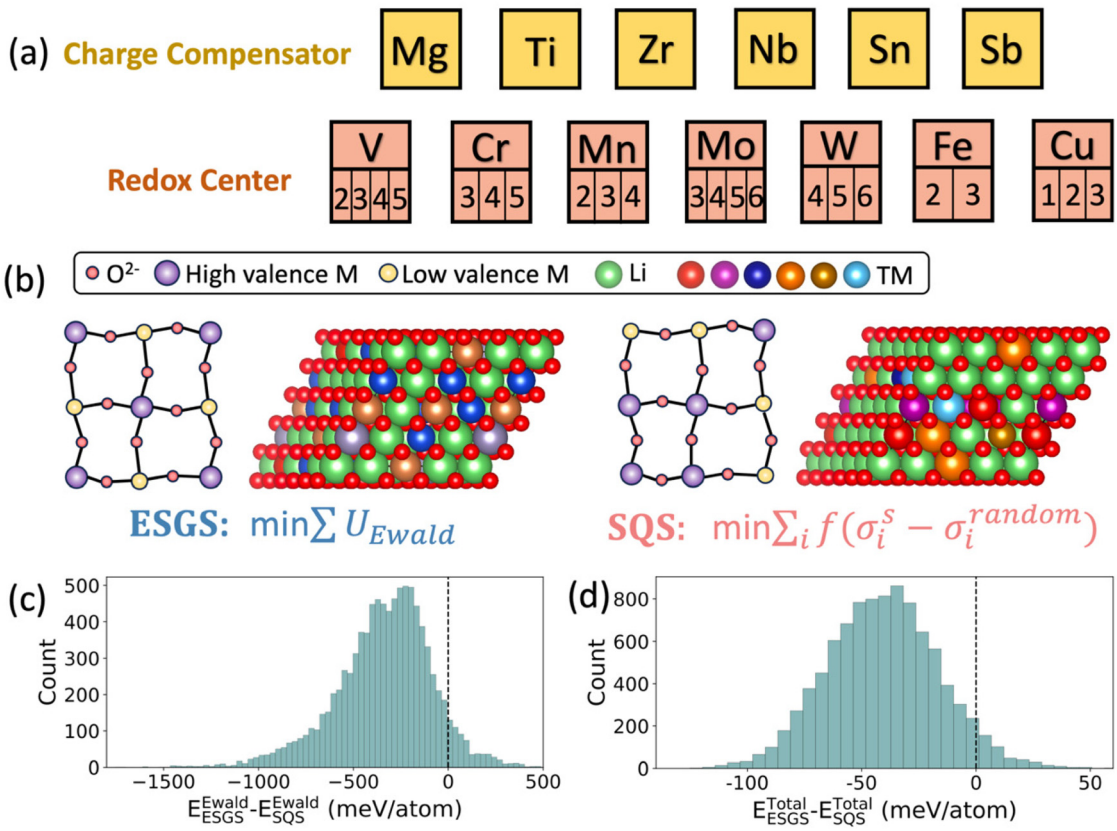

Fig. 1 (a) Selected metals in high throughput mapping Li-DRX, including six metals (Yellow color) and seven redox center metals with a total of 22 charge species (Grapefruit color). (b) Schematic of the SQS and ESGS structures for prototype composition $Li_{48}M_{32}O_{80}$. (c) The Ewald summation energy difference between ESGS structures (E^{Ewald}_{ESGS}) and SQS structures (E^{Ewald}_{SQS}) after DFT relaxation. (d) The total energy difference between ESGS (E^{Total}_{ESGS}) and SQS (E^{Total}_{ESGS}) after DFT simulations.

random limit by using special quasi-random structures, *e.g.*, SQS structures. The illustration of ESGS and SQS structures can be represented in Fig. 1(b). The detailed information for composition and structures is shown in Fig. S1. ESGS represents an ensemble of low-energy atomic configurations obtained by minimizing the Ewald summation for a given composition. This approach is motivated by our recent experimental observations,[30] which indicate that typical SRO is primarily driven by electrostatic interactions. While such structures may have limitations in capturing temperature-dependent variations in SRO, they serve as efficient and representative models of the SRO state, which is the focus of the present work.

The disordering tendency is assessed by calculating the energy difference between fully disordered states (approximated by SQS structure) and electrostatically ordered states (approximated by electrostatic ground state, *e.g.*, ESGS). The ESGS state is identified recently both from theory and experiment to be the topotactic competing phase of SRO or even medium-range ordering in DRX materials we study,[32–34] thus can be a reasonable proxy for ordered states. The claim that ESGS usually represent the energetically preferred ordering states can also be demonstrated by Fig. 1(c) and (d). The Ewald summation of ESGS structures is generally smaller than SQS structures after DFT relaxation, as the ordering is generated by minimizing the Ewald energy based on hypothetical charge states of all cations. After DFT relaxation, the relaxed charge states can change so that some ESGS end up with higher Ewald energy as shown in Fig. 1(c). As shown in Fig. 1(d), most ESGS structures show lower total energy compared to SQS structures, indicating that low energy ordering is largely driven by the tendency to minimize electrostatic energy.

3.2. The tradeoff between stability and disordering tendency

The relationship between phase stability and disordering tendency based on 9405 computed compositions can be demonstrated in Fig. 2(a). The disordering tendency is defined as the energy difference between the SQS and ESGS, denoted as E_{SQS}–E_{ESGS}. There is an obvious negative correlation between $E_{hull,1473K}$ and E_{SQS}–E_{ESGS}. The $E_{hull,1473K}$ we demonstrate here is the minimum energy between $E^{SQS}_{hull,1473K}$ and $E^{ESGS}_{hull,1473K}$, where $E^{SQS}_{hull,1473K}$ and $E^{ESGS}_{hull,1473K}$ denote the energies above hull of the SQS and ESGS configurations, respectively, evaluated at 1473 K, as the lower energy phase is more likely to be formed in experiment. To quantify the correlation between $E_{hull,1473K}$ and E_{SQS}–E_{ESGS}, we have computed the absolute value of Pearson correlation coefficient (|PCC|) to be 0.55, indicating a strong linear correlation. To further investigate the variable controlling this correlation, we plotted $E^{SQS}_{hull,1473K}$ and $E^{ESGS}_{hull,1473K}$ as functions of E_{SQS}–E_{ESGS} values, shown in Fig. 2(b) and (c). These plots clearly suggest that the linear correlation consistently appears for $E^{ESGS}_{hull,1473K}$, but is much weaker for $E^{SQS}_{hull,1473K}$. This observation indicates that the disordering tendency is closely related to the energy of the ordered states (represented by $E^{ESGS}_{hull,1473K}$) rather than the disordered states (represented by $E^{SQS}_{hull,1473K}$). In other words, a highly stable electrostatic ground state will promote ordering in HE-DRX. Such a trade-off between stability and disordering tendency is unprecedented, it suggests that one should attempt more metastable compositions for better electrochemical performance, rather than sticking with very stable compositions.

3.3. The influence of lattice distortion and charge neutrality

To explore the potential structural and compositional origins of disordering tendency, we have identified two descriptors that correlate with this preference. The first factor, illustrated in Fig. 3(a), is defined as the average deviation of the relaxed atomic positions from the rigid lattice (ε_{avg}) in the ESGS structure, calculated as the mean atomic displacement between the initial on-lattice structure and the DFT-relaxed distorted structure. As shown in Fig. 3(a), a larger ε_{avg} generally leads to more disorder, *e.g.*, smaller E_{SQS}–E_{ESGS} value. Most compositions exhi-

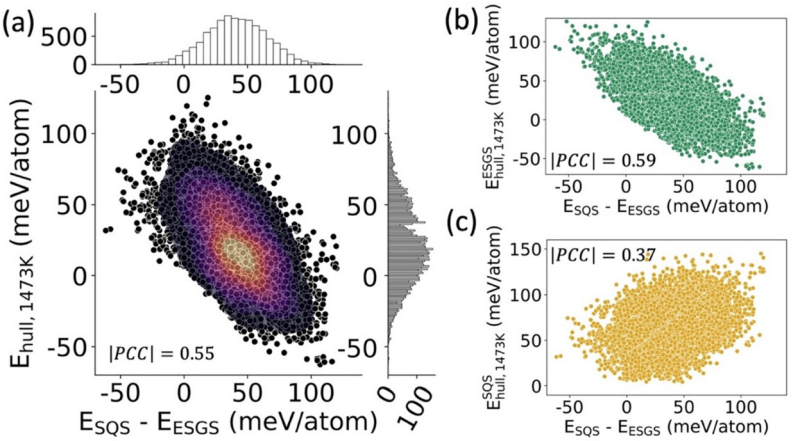

Fig. 2 (a) The trade-off between disorder tendency (E_{SQS}–E_{ESGS}) and the lower $E_{hull,1473K}$ between SQS and ESGS structures; the kernel density and the histograms represent the distribution of $E_{hull,1473K}$ and disorder tendency (E_{SQS}–E_{ESGS}). (b) A negative relation between disorder tendency (E_{SQS}–E_{ESGS}) and E_{hull} of ESGS structures at 1473K. (c) A positive relation between disorder tendency (E_{SQS}–E_{ESGS}) and E_{hull} of SGS structures at 1473K.

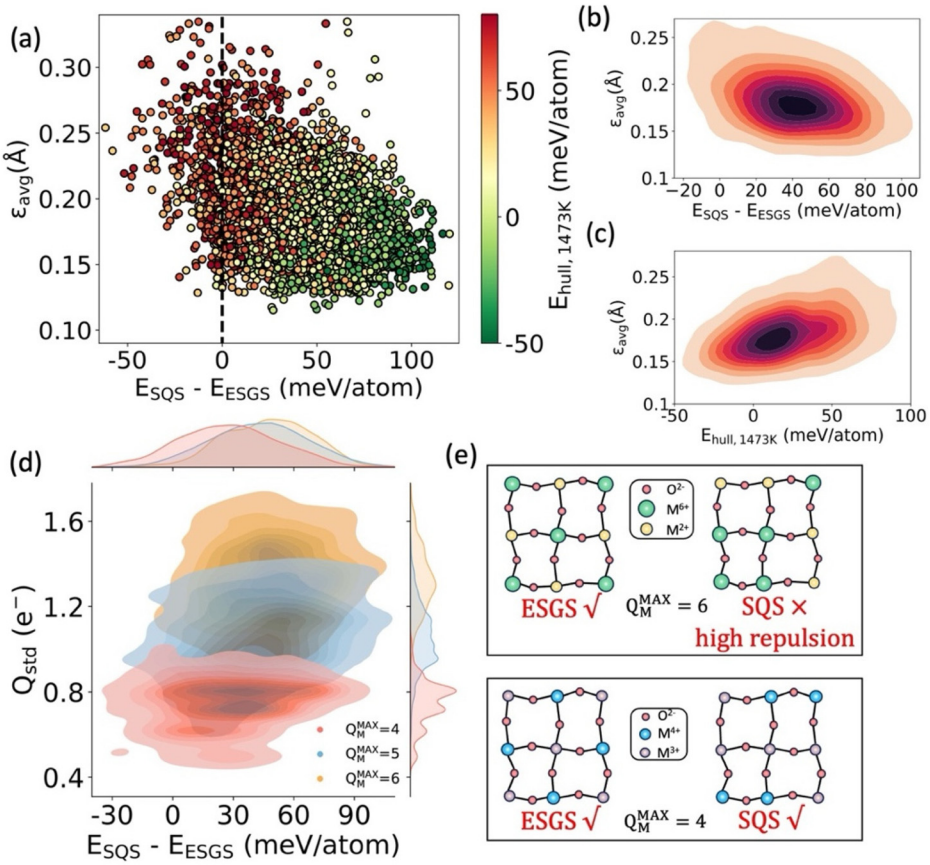

Fig. 3 (a) A scatter plot showing disorder tendency (E_{SQS}–E_{ESGS}) as a function of average off-lattice displacement with different colors representing the relative stability (*e.g.* $E_{hull,1473K}$). (b) 2D density plot showing disorder tendency (E_{SQS}–E_{ESGS}) as a function of average off-lattice displacement. (c) 2D density plot showing stability ($E_{hull,1473K}$) as a function of average off-lattice displacement. (d) The kernel distributions of disorder tendency and standard deviation of charge state (Q_{std}) at different maximum charge state of mixed transition metal (Q_M^{MAX} = 4, 5, 6). (e) A ball-stick model showing ionic occupancy in the lattice and the energy competition between two structures (SQS and ESGS).

biting a negative E_{SQS}–E_{ESGS} value have ε_{avg} greater than 0.2 Å. This trend is further clarified by Fig. 3(b). Additionally, the $E_{hull,1473K}$ value correlates positively with ε_{avg} value, which is shown in Fig. 3(c), suggesting that significant off-lattice distortion tends to destabilize the HE-DRX phase. This observation aligns with the common intuition (*e.g.* Hume–Rothery rule[35]) that off-lattice displacement and size mismatch are primary factors contributing to the instability of multi-component compounds.

In addition to lattice distortion, we have also found that the charge states of metal species also play a role in controlling disordering preference. The correlation between the standard deviation of metal charge states and E_{SQS}–E_{ESGS} value has been shown in Fig. 3(d). We categorized our data based on the maximum charge states (Q_M^{MAX}) that metal species can reach. Specifically, we considered the case when Q_M^{MAX} value is +4, +5, and +6 respectively, while Q_M^{MAX} smaller than 4 is impossible to guarantee charge balance and Li-excess simultaneously. Compositions with Q_M^{MAX} = 6 naturally exhibit a larger standard deviation of metal charge states, while those with Q_M^{MAX} = 4 show a smaller standard deviation, as demonstrated by the 2D kernel plot in Fig. 3(d) and the probability distribution on the right side. Furthermore, the probability distribution above the 2D kernel plot in Fig. 3(d) indicates that compositions with Q_M^{MAX} = 4 tend to exhibit a slightly greater disordering preference (smaller E_{SQS}–E_{ESGS}), as evidenced by the lower peak position. Conversely, compositions with Q_M^{MAX} = 6 shows larger value for E_{SQS}–E_{ESGS}. This phenomenon suggests that another strategy of promoting disorder is to minimize the standard deviation of charge states.

To visualize the physical intuition behind the relationship between metal charge states and disordering preference, we have plotted different possible orderings at various Q_M^{MAX} values in Fig. 3(e). At high Q_M^{MAX} values, local clustering of high valence metal is unfavorable due to electrostatic repulsion. This repulsion can be minimized by arranging the ions to minimize Ewald summation (the case of ESGS structure, also shown in left top panel of Fig. 3(e)). In contrast, in a fully random arrangement, certain local structures may correspond to the scenario depicted in the right top panel of Fig. 3(e). These distinct electrostatic interactions can result in a larger difference in total energy. Conversely, in the absence of high valence metals, there is much less concern about the formation of repulsive local clusters of metal ions, as illustrated by the schematic in the lower panel of Fig. 3(e).

Although variations in Li and F content may also influence the disordering tendency, such effects are indirectly accounted for by the design of the six prototype formulas, as their most direct impact is constraining the average oxidation state through charge balance.[9,10] The absence of a clear correlation between Li/F content and disordering tendency is further supported by Fig. S2 in SI. Our analysis further shows that lattice distortion and charge–state variance independently influence cation disorder (PCC = 0.25; Fig. S3), meaning they can be separately optimized. To conclude, we have indicated that in order to minimize short-range order while maximizing disordering, two viable strategies will be maximizing the lattice distortion and minimizing the charge differences of different cations. That is to say, putting multiple metals with distinct sizes can be beneficial for performance, but metals with different charge states can be harmful.

4. Discussion

4.1. Experimental verifications on disordering

To verify our computational predictions of disordering tendency, we selected two material compositions: $Li_{21}Mg_2Ti_3Zr_3Mn_4Fe_3O_{36}$ and $Li_{21}Mg_3Zr_3Mn_2Nb_3Fe_4O_{36}$ from our DFT dataset. Both materials have $2e^-$ redox from Mn per 36 O^{2-} (or per f.u.), resulting in Mn^{3+}/Mn^{4+} redox couple. These materials were selected from our high-throughput screening dataset, where the E_{SQS}–E_{ESGS} values are 22.35 meV per atom for $Li_{21}Mg_2Ti_3Zr_3Mn_4Fe_3O_{36}$ and 84.99 meV per atom for $Li_{21}Mg_3Zr_3Mn_2Nb_3Fe_4O_{36}$, respectively. Given the same Li-excess level and theoretical metal redox, both should exhibit similar initial capacities if kinetics are comparable. We synthesized and tested both materials under the same conditions to control variables. Therefore, using the initial capacity as a proxy to estimate the Li-ion extractability from the cathode materials is reasonable, which is also used in several prior work.[1,8,36,37] Although cation charge variance and lattice distortion were not explicitly considered in the initial selection, analysis shows that the more disordered composition exhibits smaller charge differences and comparable lattice distortion, as shown in Table S1, which is consistent with the disordering trends identified in our computational screening.

As indicated by Fig. 4(a), both materials are synthesized with neglectable impurities, validating that our $E_{hull,1473K}$ values (−3.49 and −35.64 meV per atom respectively) reliably capture phase stability. Through Rietveld refinement (SI Tables S2 and S3), we determine that the lattice parameters of $Li_{21}Mg_2Ti_3Zr_3Mn_4Fe_3O_{36}$ and $Li_{21}Mg_3Zr_3Mn_2Nb_3Fe_4O_{36}$ are 4.2122 and 4.2302 Å, respectively. It should be noted that both materials crystallize in a single-phase *Fm*-3*m* structure,

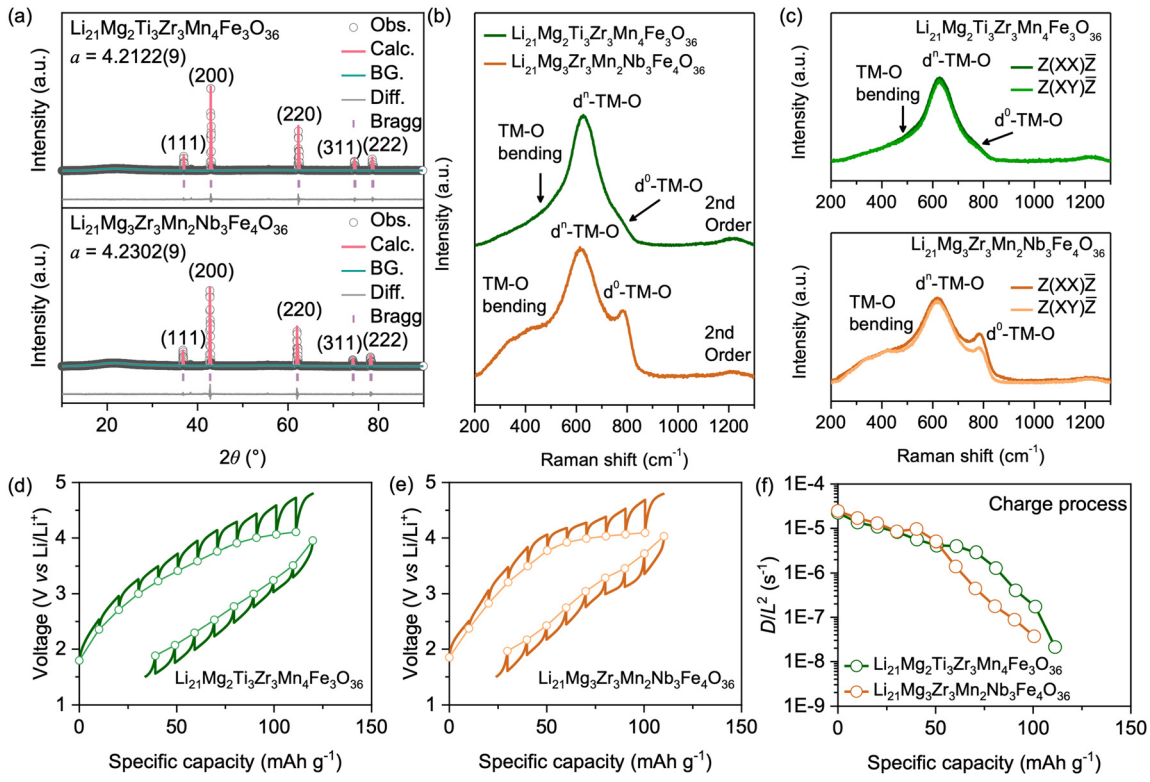

Fig. 4 Experimental realization of HE-DRXs and crystallographic and spectroscopic characterizations. (a) Rietveld refinement of XRD of $Li_{21}Mg_2Ti_3Zr_3Mn_4Fe_3O_{36}$ and $Li_{21}Mg_3Zr_3Mn_2Nb_3Fe_4O_{36}$. (b) Raman spectra and (c) polarized Raman spectra of the HE-DRXs. Second-cycle GITT profile of (d) $Li_{21}Mg_2Ti_3Zr_3Mn_4Fe_3O_{36}$ and (e) $Li_{21}Mg_3Zr_3Mn_2Nb_3Fe_4O_{36}$. (f) Calculated diffusion constant (diffusion length L^2 normalized) of the HE-DRXs for the charge process.

suggested by the negligible residue of the refinement based on the single-phase model. The single-phase nature supports the computational result that the different TM elements can be randomly dispersed in a single oxygen sublattice when a proper stoichiometry is selected, instead of crystallizing in multiple rock salt phases in which different elements are hosted. The higher lattice parameter of $Li_{21}Mg_3Zr_3Mn_2Nb_3Fe_4O_{36}$ than that of $Li_{21}Mg_2Ti_3Zr_3Mn_4Fe_3O_{36}$ is because the weighted ionic radii of TM in $Li_{21}Mg_3Zr_3Mn_2Nb_3Fe_4O_{36}$ (0.814 Å) is higher than that of $Li_{21}Mg_2Ti_3Zr_3Mn_4Fe_3O_{36}$ (0.802 Å, SI Table S4). Elemental mapping by energy-dispersive X-ray spectroscopy (SEM-EDS) (Fig. S4) confirms the homogeneous distribution of all detectable elements throughout both particles.

Besides X-ray crystallography, we examined the vibrational and electronic structure of the synthesized HE-DRXs *via* Raman spectroscopy. While rock salt structure is theoretically Raman silent, disordered rock salts often present significant Raman spectral features due to the break of perfect translational symmetry. In our previous work, we showed that Mn and Fe-based DRXs present considerable O3-layered-like features and polarization characteristics, with distinctive "E_g" (*i.e.* more depolarized) and "A_{1g}"-like (*i.e.* more polarized) symmetry.[38] Interestingly, for HE-DRXs with highly mixed d^0 and d^n TM (including Fe and Mn), the O3-layered-like features of HE-DRXs are less significant (Fig. 4b), shown as the lower intensity of TM-O bending mode (*i.e.* "E_g" band). Such an effect is more obvious for $Li_{21}Mg_2Ti_3Zr_3Mn_4Fe_3O_{36}$, in which is the TM-O bending mode is barely visible. The two high wavenumber Raman bands of the HE DRXs at 600 and 790 cm^{-1} originate from stretching-like TM-O vibration, centered at d^n-TM (*i.e.* Mn and Fe) and d^0-TM (*i.e.* Ti and Zr), respectively. Polarized Raman spectra of the HE-DRXs are shown in Fig. 4c. Agreeing with the fact that HE-DRXs demonstrate significantly less O3-layered ordering, the TM-O bending and d^n-TM-O Raman bands are largely depolarized. While the d^0-TM-O band of $Li_{21}Mg_3Zr_3Mn_2Nb_3Fe_4O_{36}$ is still moderately polarized, the d^0-TM-O band of $Li_{21}Mg_2Ti_3Zr_3Mn_4Fe_3O_{36}$ almost lost the polarization characteristics, consistent with the observation that the diminish of O3-layered ordering is more significant for $Li_{21}Mg_2Ti_3Zr_3Mn_4Fe_3O_{36}$. This nearly complete depolarization, together with the lower overall impedance and higher Li diffusion coefficient of $Li_{21}Mg_2Ti_3Zr_3Mn_4Fe_3O_{36}$, aligns with our earlier finding in DRX systems[38] that reduced local layered anisotropy facilitates Li-ion transport and increases the number of electrochemically accessible Li ions. The Raman spectroscopic observations hint that mixing TMs in a high entropy fashion diminishes short-range ordering and promotes maximal disorder, for both long-range and short-range.

Furthermore, both materials were cycled in half cells with a Li foil counter electrode, as shown in Fig. S5. The voltage curves for the initial cycle, shown in Fig. S5(a), reveal a notable difference in both charge and discharge states. It is worth noting that these two materials have theoretical metal redox capacities of 34.0 and 31.9 mAh g^{-1}, corresponding to the extraction of 2 Li per 36 O^{2-}. It's consistent with the voltage profiles of the two compounds, which demonstrate very limited capacity contribution by the sloped region toward 4.0 V (*i.e.* the region corresponding to Mn^{3+}–Mn^{4+} oxidation). However, as indicated in the voltage curve (Fig. S5(a)), 16.42 and 12.06 Li have been extracted per 36 O^{2-}, reflecting a pronounced amount of oxygen redox. The substantial oxygen redox suggests desirable Li kinetics, with $Li_{21}Mg_2Ti_3Zr_3Mn_4Fe_3O_{36}$ exhibiting notably higher charge and discharge capacities compared to $Li_{21}Mg_3Zr_3Mn_2Nb_3Fe_4O_{36}$. Differential capacity (dQ/dV) curve indicates that the oxidation voltage of $Li_{21}Mg_2Ti_3Zr_3Mn_4Fe_3O_{36}$ is slightly lower than $Li_{21}Mg_3Zr_3Mn_2Nb_3Fe_4O_{36}$, hinting slightly faster Li deintercalation kinetics for $Li_{21}Mg_2Ti_3Zr_3Mn_4Fe_3O_{36}$. In addition, 2^{nd}-cycle galvanostatic intermittent titration (GITT) profiles were measured and shown in Fig. 4(d)–(f). The calculated diffusion constants for $Li_{21}Mg_2Ti_3Zr_3Mn_4Fe_3O_{36}$ are slightly larger than those of $Li_{21}Mg_3Zr_3Mn_2Nb_3Fe_4O_{36}$. Because of the substantial contribution of oxygen oxidation and limited TM redox contribution, consequently, both materials show much larger charge capacities compared to discharge capacities due to irreversible oxygen redox. Continuous cycling (Fig. 5 and Fig. S7) further supports this, showing that ongoing oxygen-redox-induced degradation gradually diminishes the initial kinetic advantage. Rate capability tests over current densities from 10 mA g^{-1} to 1 A g^{-1} (Fig. 5 and Fig. S7) reveal that $Li_{21}Mg_2Ti_3Zr_3Mn_4Fe_3O_{36}$ consistently outperforms $Li_{21}Mg_3Zr_3Mn_2Nb_3Fe_4O_{36}$ across all rates, with particularly pronounced benefits under high-rate conditions, where it also demonstrates superior cycling stability. At a low rate of 10 mA g^{-1}, $Li_{21}Mg_2Ti_3Zr_3Mn_4Fe_3O_{36}$ stabilizes at ~90 mAh g^{-1} within ~6 cycles, whereas $Li_{21}Mg_3Zr_3Mn_2Nb_3Fe_4O_{36}$ requires ~15 cycles to stablize at ~65 mAh g^{-1}, indicating faster kinetics in the $Li_{21}Mg_2Ti_3Zr_3Mn_4Fe_3O_{36}$.

EIS measurements using a BioLogic workstation evaluated cell impedance at OCV and after 20 cycles for both HE-DRX cathodes are shown in Fig. S8. For $Li_{21}Mg_2Ti_3Zr_3Mn_4Fe_3O_{36}$, the impedance increased from ~55 Ω (pristine) to ~80 Ω (after 20 cycles), while for $Li_{21}Mg_3Zr_3Mn_2Nb_3Fe_4O_{36}$, it increased from ~70 Ω to ~95 Ω. Although both cathodes exhibit an increase in impedance upon cycling, $Li_{21}Mg_2Ti_3Zr_3Mn_4Fe_3O_{36}$ consistently shows lower impedance values, which aligns well with its superior electrochemical performance discussed above.

Based on these experimental observations, both our stability descriptor E_{hull} and disordering descriptor E_{SQS}–E_{ESGS} are confirmed to be effective for predicting the initial electrochemical performance of cathodes. Such experimental verifications also reveal that a practical way of designing more disordered HE-DRX is trying to incorporate cations with large size difference while minimizing the variation of charge states of such cations. Some of the design principles identified here, such as promoting moderate lattice distortion and ensuring charge-state compatibility, may also be relevant to other cathode families, including layered oxides. However, the descriptors for good rate performance in these systems may differ from those used for DRX cathodes (*e.g.*, 0TM percola-

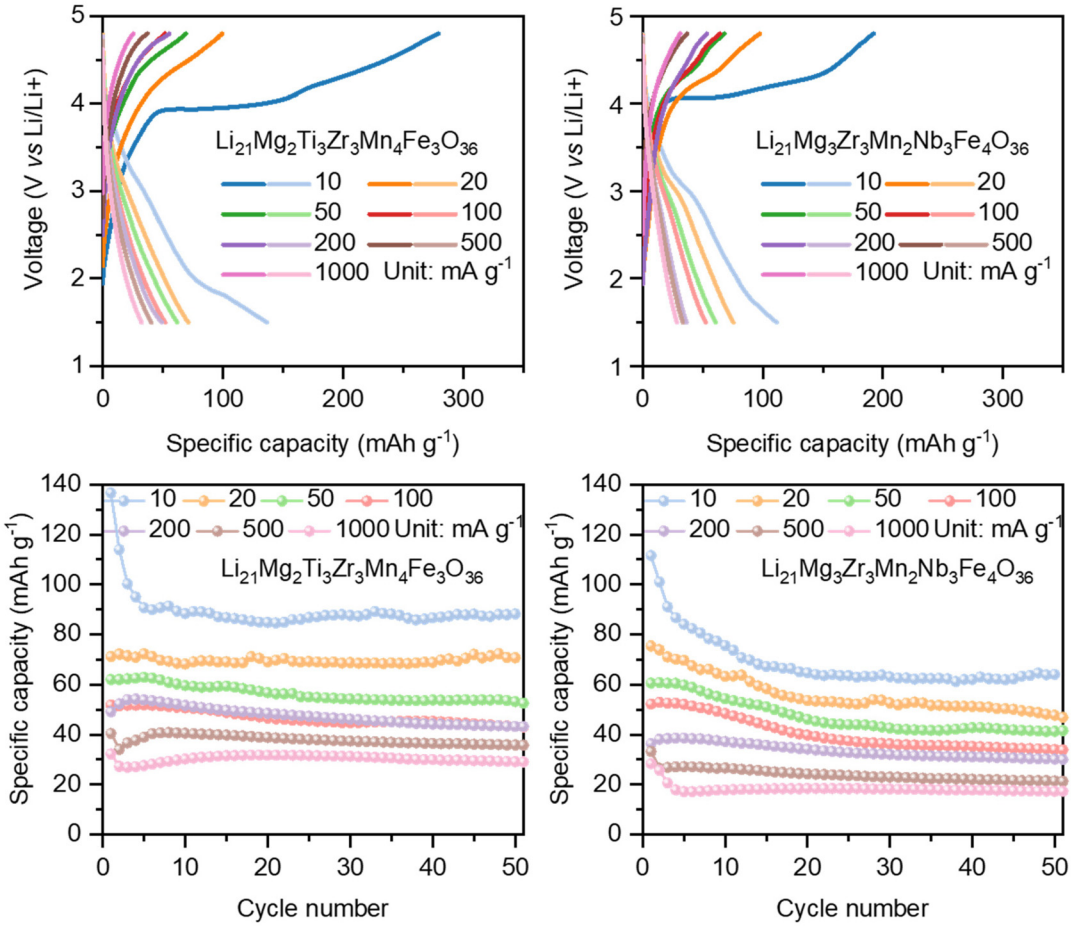

Fig. 5 The first-cycle voltage profiles of (a) $Li_{21}Mg_2Ti_3Zr_3Mn_4Fe_3O_{36}$ and (b) $Li_{21}Mg_3Zr_3Mn_2Nb_3Fe_4O_{36}$ under different current densities. Discharge specific capacity retention of (c) $Li_{21}Mg_2Ti_3Zr_3Mn_4Fe_3O_{36}$ and (d) $Li_{21}Mg_3Zr_3Mn_2Nb_3Fe_4O_{36}$ over 50 cycles under different current densities.

tion). We therefore recommend further investigation before directly extending the conclusions of this work.

Conflicts of interest

The authors declare no competing financial interest.

Data availability

The data supporting the research are available within the main text and SI. Additional data analysis and experiment result including SEM-EDS, voltage profiles, and EIS measurements are displayed in the SI. More raw data can be made available upon request.

Supplementary information is available. See DOI: **https://doi.org/10.1039/d5eb00104h**.

Acknowledgements

L. W., Z. H., and B. O. would like to acknowledge funding support from Samsung Global Research Opportunity. The Computational resources are provided by the Advanced Cyberinfrastructure Coordination Ecosystem: Services & Support (ACCESS), the National Energy Research Scientific Computing Center (NERSC), a DOE Office of Science User Facility supported by the Office of Science and the U.S. Department of Energy under contract no. DE-AxC02-05CH11231 and Research Computing Center (RCC) at Florida State University. The computation and data processing are also supported by the supercomputing resources from the Department of Energy's Office of Energy Efficiency and Renewable Energy at the National Renewable Energy Laboratory.

References

1 Z. Lun, B. Ouyang, D. H. Kwon, Y. Ha, E. E. Foley, T. Y. Huang, Z. Cai, H. Kim, M. Balasubramanian, Y. Sun, J. Huang, Y. Tian, H. Kim, B. D. McCloskey, W. Yang, R. J. Clement, H. Ji and G. Ceder, *Nat. Mater.*, 2021, **20**, 214–221.
2 B. Ouyang and Y. Zeng, *Nat. Commun.*, 2024, **15**, 973.
3 S. Zhou, Y. Sun, T. Gao, J. Liao, S. Zhao and G. Cao, *Angew. Chem., Int. Ed.*, 2023, **62**, e202311930.

4 L. Wang, Z. D. He and B. Ouyang, *Comput. Mater. Sci.*, 2023, **230**, 112513.
5 K. Mizushima, P. C. Jones, P. J. Wiseman and J. B. Goodenough, *Mater. Res. Bull.*, 1980, **15**, 783–789.
6 A. Manthiram, *Nat. Commun.*, 2020, **11**, 1550.
7 Z. Cai, Y. Q. Zhang, Z. Lun, B. Ouyang, L. C. Gallington, Y. Sun, H. M. Hau, Y. Chen, M. C. Scott and G. Ceder, *Adv. Energy Mater.*, 2022, **12**, 2103923.
8 Z. Y. Lun, B. Ouyang, Z. J. Cai, R. Clément, D. H. Kwon, J. P. Huang, J. K. Papp, M. Balasubramanian, Y. S. Tian, B. D. McCloskey, H. W. Ji, H. Kim, D. A. Kitchaev and G. Ceder, *Chem*, 2020, **6**, 153–168.
9 B. Ouyang, N. Artrith, Z. Lun, Z. Jadidi, D. A. Kitchaev, H. Ji, A. Urban and G. Ceder, *Adv. Energy Mater.*, 2020, **10**, 1903240.
10 H. Ji, A. Urban, D. A. Kitchaev, D. H. Kwon, N. Artrith, C. Ophus, W. Huang, Z. Cai, T. Shi, J. C. Kim, H. Kim and G. Ceder, *Nat. Commun.*, 2019, **10**, 592.
11 J. H. Liao, H. Chen, Y. S. Xie, Z. H. Li, S. D. Tan, S. Y. Zhou, L. Jiang, X. Zhang, M. Liu, Y. B. He, F. Y. Kang, Z. Y. Lun, S. X. Zhao and T. Z. Hou, *Adv. Energy Mater.*, 2025, 2501857.
12 A. Zunger, S. Wei, L. G. Ferreira and J. E. Bernard, *Phys. Rev. Lett.*, 1990, **65**, 353–356.
13 L. Wang and B. Ouyang, *Adv. Mater.*, 2024, **36**, e2307860.
14 A. Urban, I. Matts, A. Abdellahi and G. Ceder, *Adv. Energy Mater.*, 2016, **6**, 1600488.
15 A. Urban, A. Abdellahi, S. Dacek, N. Artrith and G. Ceder, *Phys. Rev. Lett.*, 2017, **119**, 176402.
16 A. Abdellahi, A. Urban, S. Dacek and G. Ceder, *Chem. Mater.*, 2016, **28**, 3659–3665.
17 A. Abdellahi, A. Urban, S. Dacek and G. Ceder, *Chem. Mater.*, 2016, **28**, 5373–5383.
18 G. Kresse and D. Joubert, *Phys. Rev. B: Condens. Matter Mater. Phys.*, 1999, **59**, 1758–1775.
19 G. Kresse and J. Furthmuller, *Comput. Mater. Sci.*, 1996, **6**, 15–50.
20 S. L. Dudarev, G. A. Botton, S. Y. Savrasov, C. J. Humphreys and A. P. Sutton, *Phys. Rev. B: Condens. Matter Mater. Phys.*, 1998, **57**, 1505–1509.
21 L. Wang, T. Maxisch and G. Ceder, *Phys. Rev. B: Condens. Matter Mater. Phys.*, 2006, **73**, 195107.
22 A. Jain, S. P. Ong, G. Hautier, W. Chen, W. D. Richards, S. Dacek, S. Cholia, D. Gunter, D. Skinner, G. Ceder and K. A. Persson, *APL Mater.*, 2013, **1**, 011002.
23 G. Hautier, C. Fischer, V. Ehrlacher, A. Jain and G. Ceder, *Inorg. Chem.*, 2011, **50**, 656–663.
24 W. Sun, S. T. Dacek, S. P. Ong, G. Hautier, A. Jain, W. D. Richards, A. C. Gamst, K. A. Persson and G. Ceder, *Sci. Adv.*, 2016, **2**, e1600225.
25 B. Ouyang, J. Wang, T. He, C. J. Bartel, H. Huo, Y. Wang, V. Lacivita, H. Kim and G. Ceder, *Nat. Commun.*, 2021, **12**, 5752.
26 L. Wang, J. Wang and B. Ouyang, *Adv. Energy Mater.*, 2023, **13**, 2302584.
27 V. Murray, D. S. Hall and J. R. Dahn, *J. Electrochem. Soc.*, 2019, **166**, A329–A333.
28 R. J. Clément, Z. Lun and G. Ceder, *Energy Environ. Sci.*, 2020, **13**, 345–373.
29 L. Wang, N. Sunariwal, Y. He, D.-h. Kim, D.-h. Yeon, Y. Zeng, J. Cabana and B. Ouyang, *Adv. Energy Mater.*, 2025, **15**, 2404982.
30 L. Li, B. Ouyang, Z. Lun, H. Huo, D. Chen, Y. Yue, C. Ophus, W. Tong, G. Chen, G. Ceder and C. Wang, *Nat. Commun.*, 2023, **14**, 7448.
31 J. Lee, D. A. Kitchaev, D.-H. Kwon, C.-W. Lee, J. K. Papp, Y.-S. Liu, Z. Lun, R. J. Clément, T. Shi, B. D. McCloskey, J. Guo, M. Balasubramanian and G. Ceder, *Nature*, 2018, **556**, 185–190.
32 L. Li, B. Ouyang, Z. Lun, H. Huo, D. Chen, Y. Yue, C. Ophus, W. Tong, G. Chen, G. Ceder and C. Wang, *Nat. Commun.*, 2023, **14**, 7448.
33 Z. Cai, B. Ouyang, H.-M. Hau, T. Chen, R. Giovine, K. P. Koirala, L. Li, H. Ji, Y. Ha, Y. Sun, J. Huang, Y. Chen, V. Wu, W. Yang, C. Wang, R. J. Clément, Z. Lun and G. Ceder, *Nat. Energy*, 2023, **9**, 27–36.
34 L. Wang, T. He and B. Ouyang, *ACS Mater. Lett.*, 2025, 2708–2715, DOI: **10.1021/acsmaterialslett.5c00726**.
35 R. Hultgren and L. Tarnopol, *Nature*, 1938, **141**, 473–474.
36 H. Ji, A. Urban, D. A. Kitchaev, D.-H. Kwon, N. Artrith, C. Ophus, W. Huang, Z. Cai, T. Shi, J. C. Kim, H. Kim and G. Ceder, *Nat. Commun.*, 2019, **10**, 592.
37 B. Ouyang, N. Artrith, Z. Lun, Z. Jadidi, D. A. Kitchaev, H. Ji, A. Urban and G. Ceder, *Adv. Energy Mater.*, 2020, **10**, 1903240.
38 Y. Wang, S. Huang, B. Raji-Adefila, A. Outka, J.-H. Wang and D. Chen, *J. Am. Chem. Soc.*, 2022, **144**, 19838–19848.